Marine Research
of the National Academy of Marine Research
ISSN: 2709-6629 (Vol.2 Iss.2)
GPN: 2011200033

DOI: http://dx.doi.org/10.29677/MR.202212_2(2).0004
2022, 2(2), 58-74

Study On the Coastal Thermal Plume Patterns by the Land-based X-band Radar Images

Li-Chung Wu [1*] Laurence Zsu-Hsin Chuang [2] Dong-Jiing Doong [1,3]

[1] *Coastal Ocean Monitoring Center, National Cheng Kung University, Tainan, Taiwan*
[2] *Institute of Ocean Technology and Marine Affairs, National Cheng Kung University, Tainan, Taiwan*
[3] *Department of Hydraulic and Ocean Engineering, National Cheng Kung University, Tainan, Taiwan*

ABSTRACT

An oceanic thermal plume, which is often induced by the discharge of heated wastewater, is unavoidable in the coastal area around a power plant. We studied the patterns of thermal plumes from sea surface images of land-based X-band radar images. By averaging the image sequences, we were able to eliminate the patterns of wave crests and detect a band of strong radar echo intensity in front of the drain outlet of a power station. Field temperature records confirm the relationship between this echo band and the thermal plume. We learned that the movement features of the thermal plume in our study site are often influenced by tidal currents. Air-sea temperature differences and wind both significantly enhance the intensity of the radar echo. However, the influences of strong wind speed and upwind conditions are more sensitive with respect to enhancing the pattern of the thermal plume discharge from the X-band radar sea surface images.

Keywords: thermal plume, land-based X-band radar, sea surface.

---

* Corresponding author, E-mail: jackalson18@gmail.com

Received 3 August 2022, Accepted 11 October 2022.

1 INTRODUCTION

Coastal zones, which are often densely populated regions throughout the world, exert a continuously increasing influence on global economic activities. Due to frequent economic and industrial development within these areas, the discharge of heated wastewater from coastal power plants and factories is often unavoidable. To operate a coastal power plant, especially in the cases of thermal and nuclear power, the release of thermal energy through the plant's heat exchangers into the ocean is common. Heated effluent water is chemically inoffensive, but it is sufficiently warm and in such quantity as to considerably change the coastal water temperature near the power plant. Half a century ago, there were several studies focused on the possible effects of thermal effluents on fish (Miller, 1977; Sylvester, 1972).

We cannot ignore interactions between the thermal effluent and environmental factors. Thermal plume dynamics are quite complicated in coastal waters due to the interactions of bathymetry, waves, tides, and currents. For complete coastal management, thermal effluent discharge information is vital to understanding the impact of waste heat on the coastal environment. Different approaches have been proposed to obtain thermal effluent information in coastal areas. Based on the development of hydrodynamic theories and numerical methods, a numerical model is a useful tool to simulate the thermal effluent under the influences of different environmental factors (Joongcheol, 2011). The simulated results of thermal plume are often compared to field data to verify the feasibility of the model (Yanagi et al., 2005). However, a complete and intensive field measurement is always a difficult task, especially for obtaining plume information in the spatial domain. Yanagi et al. (2005) deployed 117 sea surface temperature (SST) stations and 25 conductivity-temperature-depth (CTD) stations within an area of approximately 0.4°×0.4°. A field experimental arrangement like this is very helpful for obtaining the distribution of heated water in the spatial domain. However, the concomitant costs of the field experiment are also considerable.

Remote sensing is superior to in-situ measurements for detecting the spatial patterns of a thermal plume. Airborne and satellite-based technologies have been used to detect surface thermal plumes in different studies. Satellite measurements of surface temperature are an ideal way to apply this approach in a dynamic estuarine environment (Mustard et al., 1999). For the study of Mustard et al. (1999), the spatial resolution of each picture element (pixel) on the surface in the thermal channel is 120 m × 120 m. The study of these images focused on the patterns of thermal properties across large spatial scales. On the other hand, to detect and study the spatial patterns of small-scale thermal plumes, it is necessary to implement other remote sensing techniques.

Nautical X-band radar, originally used on ships for safety at sea and near the shore, is currently one of the most popular tools for remote ocean sensing. Based on the sensitivity of X-band on the rough sea surface, several studies revealed the features of radar echo intensity under different environmental factors (Frasier et al., 1998; Lee et al., 1998; Trizna et al., 1991). In applying this approach to sea state monitoring, Young et al. (1985) were pioneers in extracting information about ocean waves and sea surface currents from the wave patterns on X-band radar images. In addition to its application to sea state observations, other studies revealed that sea surface patterns are related to different physical phenomena, such as internal waves and river plumes situated in front of estuaries (Ramos et al., 2009; Robinson et al., 2000; Sletten et al., 1999).

Robinson et al. (2000) suggested the hypothesis that pipe-flow discharge reaches the surface and in some way alters the roughness detected by radar. Thus far most of the studies on plume detection by remote sensing have focused on river discharges. For thermal effluents from thermal power stations, we previously observed microscale (less than 1 km) thermal plume patterns from land-based X-band radar sea surface images (Bau et al., 2013). Although other studies have investigated the physics of radar backscatter across mesoscale sea

DOI: 10.29677/MR.202212_2(2).0004

surface temperature fronts by airborne X-band radar observations (Askari et al., 1993), we focused on the nearshore microscale thermal plume using low-angle grazing radar. Compared to shipboard or airborne radar, the land-based radar system permits continuous and long-term monitoring. The superiority of land-based X-band radar for detecting the thermal plume can provide spatiotemporal information about the sea surface. Both the spatial distribution of the thermal plume and its motion features can be extracted from spatiotemporal sea surface images. The aim of our study is to discuss patterns of the nearshore thermal plume from sea surface images of land-based X-band radar. Field radar images with simultaneous meteorological and sea-state data were also collected and analyzed in our study to ascertain plume patterns under different environmental parameters.

2 EXPERIMENTAL ARRANGEMENT

The images in our study showing thermal plume patterns were collected from the coastal area of western Taiwan. The horizontally oriented radar antenna is at an altitude of 15 m. Because the thermal plume is at least 500 m from the radar antenna, the radar grazing angle is less than 2°. This is the low grazing angle that plays a specific role in the scattering of electromagnetic microwaves by a rough sea surface (Kanevsky, 2008). For the image cases in our study, 64 continuous radar image sequences with a 7.5-m/pixel spatial resolution are acquired for each measurement. The radar device is equipped with a 42-rpm antenna, which yields an image sequence sampling rate of 0.7 Hz. Figure 1(a) shows the sea area of our experiment, which is close to Hsinta Power Plant in Taiwan. The radar monitoring area is marked by a dashed circle. The arrow in the figure indicates the direction of the plume at the power station drain outlet.

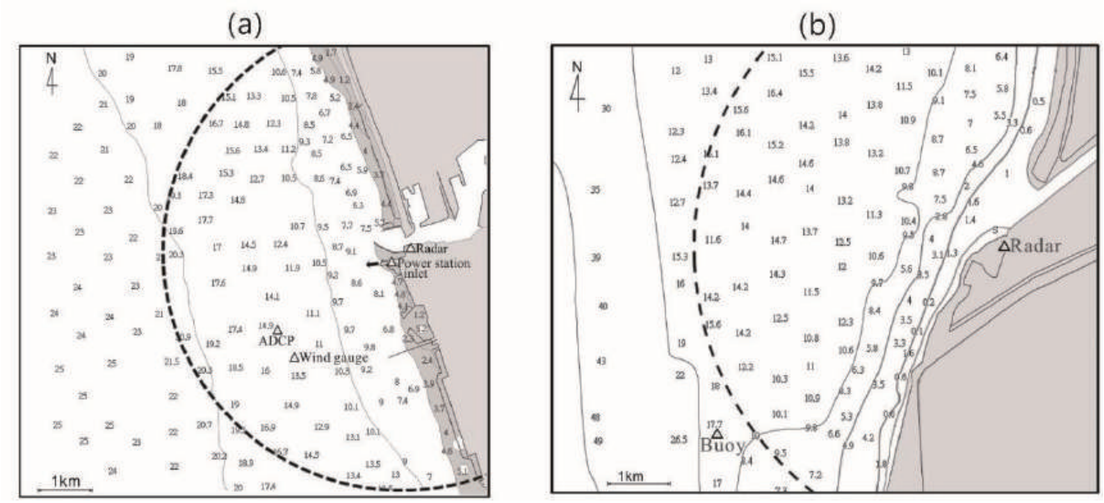

Figure 1. Experimental sites in our study (water depths in meters).

Approximately 3,000 image cases from the experimental site shown in Figure 1(a) were used in this study. To verify the features from the sea surface radar images, we used simultaneous in-situ wave and current data obtained from a bottom-mounted ADCP (acoustic Doppler current profiler). Simultaneous wind data were also measured on a pier in our study. However, the available sea surface temperature data in the experimental site of Figure 1(a) included only several hours of records measured from a small boat. Long-term sea surface temperature data are also quite important for the study of sea echo backscattering. Hence, we installed the same radar system in the experimental site of Figure 1(b), which is near an operational data buoy. Figure 1(b) shows the Qigu sea area near Tainan, Taiwan. Although the distance between the locations of the in-situ moored buoy and the radar monitoring area is approximately 3 km, the air and near sea surface temperature data from the moored buoy may still be useful for our study under the assumption of homogeneous sea states. Long-term and stable temperature records are helpful for interpreting the influence of environmental temperatures on sea surface backscattering. More than 2,000 image cases were collected from the experimental area of Figure 1(b). Note that there is no thermal plume within this area. The image data from Figure 1(b) are only used to discuss the correlation between temperature and sea echoes of the X-band radar.

3 IMAGE PROCESSING FOR DETECTING THERMAL PLUME FEATURES

The first step in extracting the plume pattern is to decrease the pattern of ocean waves. Coastal wave patterns are often obvious because of strong backscattering from the wave crests and the influence of wave shadowing (Borge et al., 2004). Due to the phenomenon of wave propagation, it is possible to eliminate patterns of waves or swells from sea surface images by averaging the image sequences in the time domain. In this study we used the average of 64 continuous radar image sequences from each observation. This means that a sequence of images is averaged over 90 sec. Wind-generated waves have a range of periods from about 1 to 30 sec. When a sequence of images is averaged over a period substantially longer than the period of wind-generated waves, the backscatter variations from the waves are averaged out, leaving a mean backscatter image in which there are areas of consistently higher backscatter (Ruessink et al., 2002), such as thermal plume patterns.

In addition to the noise from ocean waves on the sea surface image, the decay of the radar signal with increasing distance also influences radar imaging. According to the radar equation, radar echo intensity is related to the distance R between the target and the radar antenna. The power of the signal reflected from the target and received by the radar is proportional to R^{-4} (Richards, 2005). However, the thermal plume patterns at the area near the radar antenna are eliminated if we multiply the radar echo intensity by R^4 . Because the thermal plume patterns on our radar image cases are all within 4.5 km of the radar antenna, the thermal plume patterns within this range are clear enough to be recognized. Thus we do not have to address the decay effect resulting from increasing distance.

To quantify the radar backscatter from the averaged images, we normalized the radar echo intensity as follows:

$$I_n(x,y)=I(x,y)/I_{max} \tag{1}$$

where $I(x,y)$ is the original averaged radar echo intensity at different spatial locations (x,y),$I_n(x,y)$ is the normalized result from $I(x,y)$, and I_{max} is the maximal value of the entire $I(x,y)$. Note that the maximal values of the different image cases are always at the location of the radar antenna. Because all the radar backscatter images are obtained from the same radar system, the values of I_{max} are also nearly the same among the different image cases.

Figure 2 presents one of our radar image cases. In addition to the radar backscatter from coastal engineering structures (pier and breakwater), a radar echo band also appears in the middle part of the radar image. One end of this radar echo band is at the drain outlet of the power plant. In this case, we can see that this radar echo band bends to the north. During the observation period of this case, we also have the simultaneous in-situ sea surface temperature data, which were measured from a small boat. Figure 2(a) shows the results when we nest the sea surface temperature contours on the sea surface image. The sea surface temperature data confirm that higher water temperature is distributed at the zone of the drain outlet and that warmer water is directed to the north. The difference between the temperature of the warmest water and averaged temperature data can be as much as 3°C. The results of Figure 2(a) confirm that the area of the radar echo band mentioned above is located within this warm water zone. It is possible to detect the thermal plume from the averaged X-band radar images.

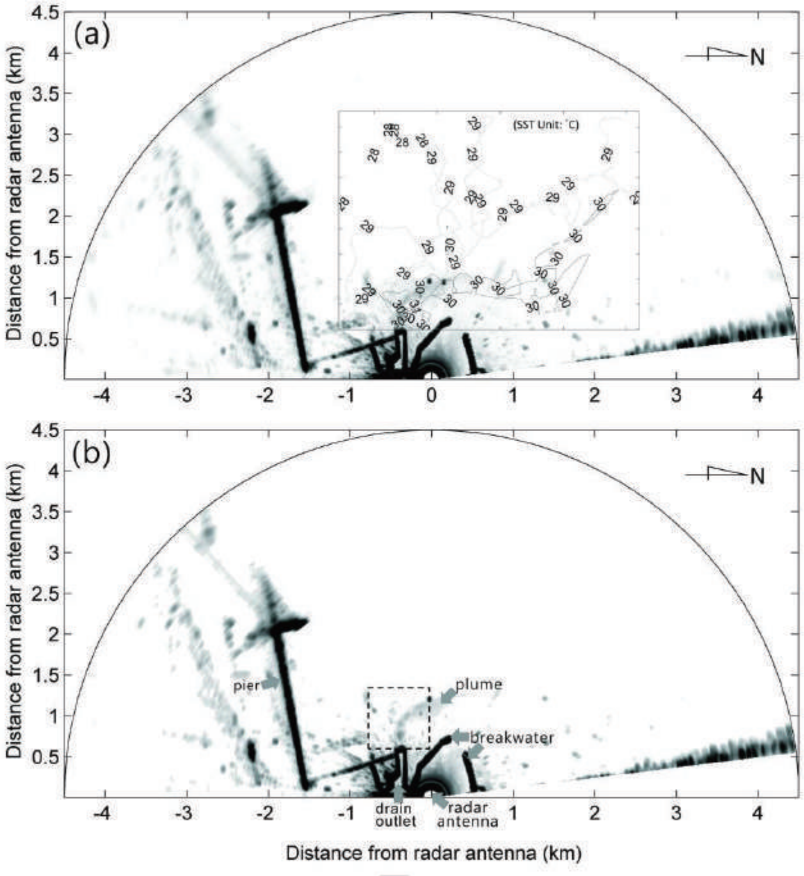

Figure 2. (a) One radar image case and its simultaneous sea surface temperature information; (b) The same image case indicating the area of the thermal plume (marked by the dashed frame).

4 MOVING FEATURES OF THE THERMAL PLUME

We can confirm the relationship between the radar echo band of the thermal plume and the distribution of warmer water in the coastal area (Figure 2). Here, we try to recognize the moving features of the thermal plume by use of continuous sea surface image cases. Figure 3 presents the continuous 24-hour sub-images extracted from the area we marked in Figure 2(b). The images show that the radar echo band oscillates with time. The radar echo bands bending to the north are stronger than those bending to the south. As shown in Figure 2, the radar antenna is located north of the drain outlet. The distances between the radar antenna and the thermal plume bending to the south are larger. Because the received electromagnetic energy obeys a decay law with increasing distance, the intensity values of the echo band are stronger at the north of the drain outlet.

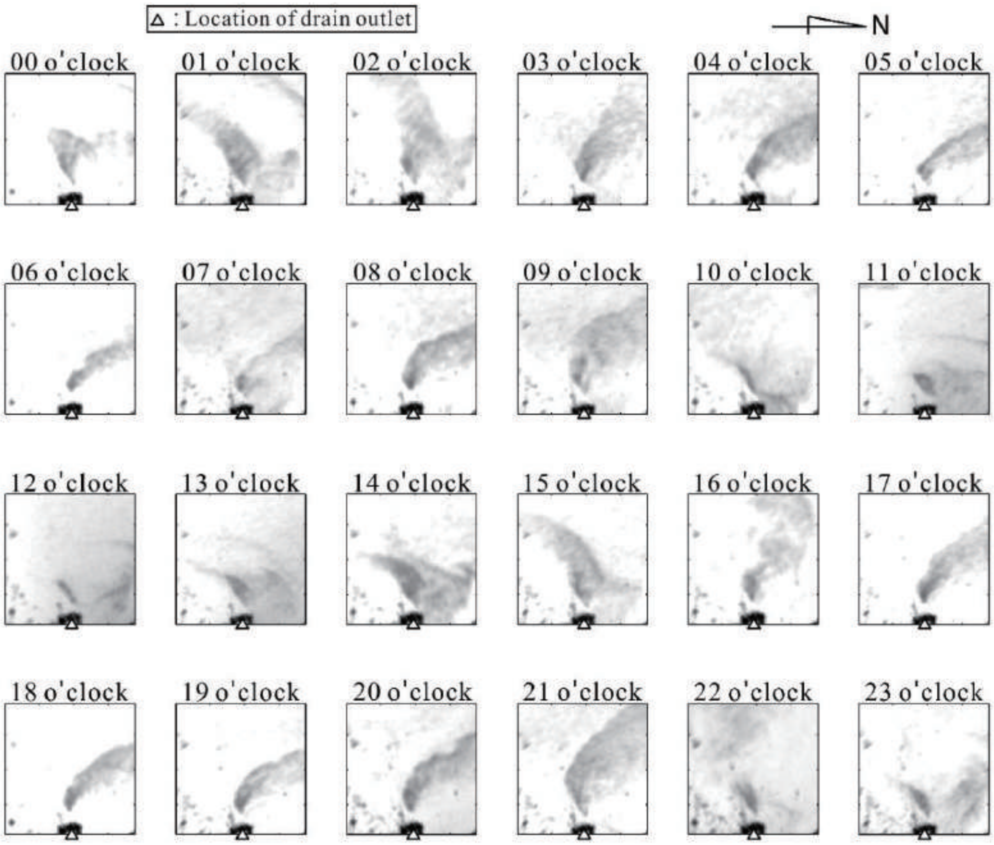

Figure 3. Image cases of the thermal plume features within a continuous 24-hour period.

From the images of Figure 3, we can more easily identify the radar echo band of the thermal plume. For the sub-image cases at 04, 05, 06, 07, 08, 17, 18, 19 and 20 o'clock, the radar echo bands of these cases bend toward the north; we classified these images as cases (A). However, the radar echo bands from the sub-image cases at 10, 11, 12, 13, 14, 15, 22, and 23 o'clock bend from the drain outlet towards the south; we classified these images as cases (B). From the motion of the radar echo band, we can confirm that the thermal plume flows both northward and southward approximately twice daily.

To interpret the moving features of the thermal plume, simultaneous in-situ current measurements from an upward looking ADCP were analyzed. Figure 4 shows the time series of the near sea surface current speed and direction. To define the current direction, 0° is a current flowing from south to north, and 90° is one flowing from west to east. This experimental site is located within the Taiwan Strait and is oriented nearly north and south. Due to this geographical feature, the tidal current often flows to the north during the flood stream and to the south during the ebb stream. Figure 5 presents the near sea surface current ellipses which were analyzed from the ADCP records. The near sea surface current is mainly dominated by the tidal constituents of M2, K1, S2 and O1. The current ellipses showed that the principal axes of these tidal constituents are close to N-S or NW-SE.

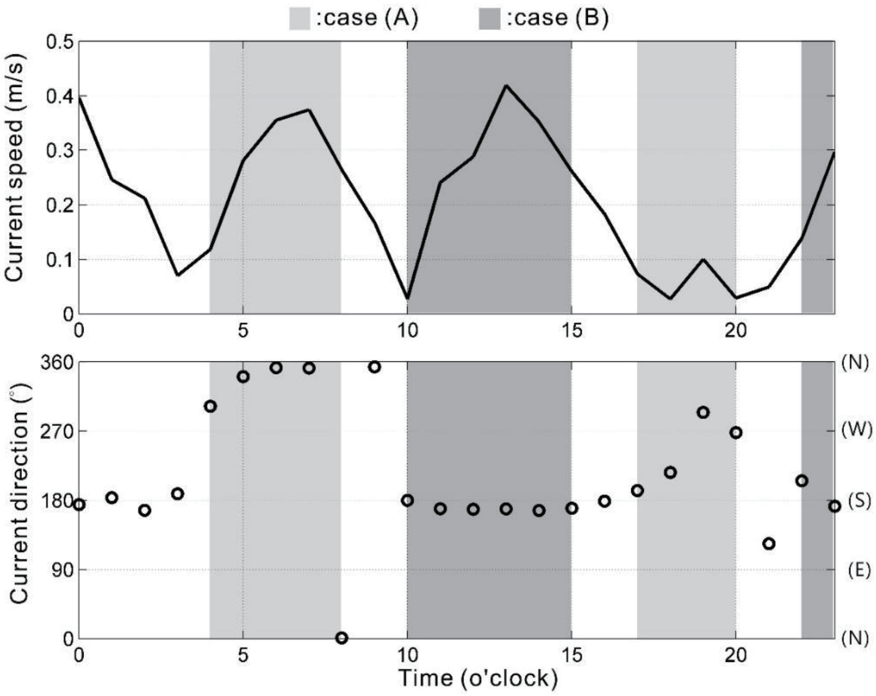

Figure 4. Near sea surface current data measured from the ADCP.

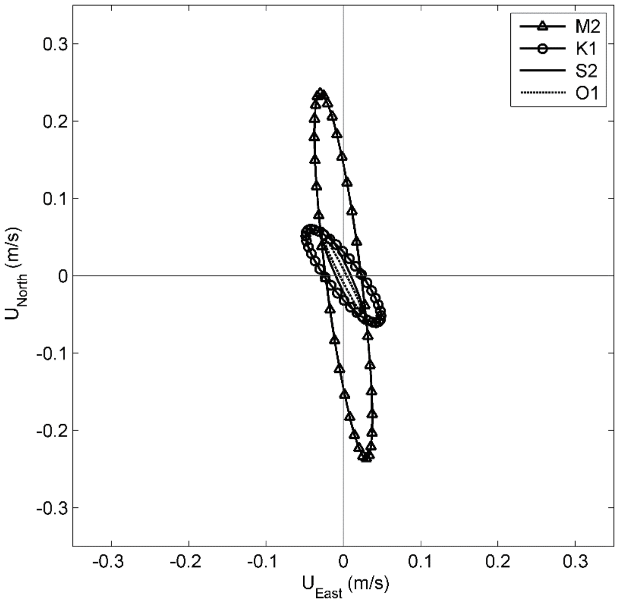

Figure 5. Near sea surface current ellipses analyzed from the ADCP records.

The plume motion should be influenced by the tidal current. To study the relationship between the surface current and plume motion, the time ranges of cases (A) and (B) are both marked on Figure 4. During the 04, 05, 06, 07 and 08 o'clock periods of cases (A), the in-situ current directions are approximately 0° but are not close to north at 17, 18, 19 and 20 o'clock. Note that the current speeds in this duration are lower than 0.1 m/s. The sea surface current did not dominate the motion of thermal plume under this weaker sea current. Compared to cases (A), cases (B) often occur while the current directions obtained from the ADCP are approximately 180°.

To confirm the influence of the sea surface on the motion of the thermal plume, we evaluated the image cases in which the radar echo bands bend toward the north and south. Figures 6(a) and 6(b) show the simultaneous in-situ current information for the radar echo bands bending toward the north and the south, respectively. When the radar echo bands bend toward the north, the sea surface currents often also flow to the north. When surface current directions are not close to north, the current speeds are always weaker. Figure 6(b) shows similar results. We confirm that the motions of the thermal plume are mainly influenced by the near sea surface current.

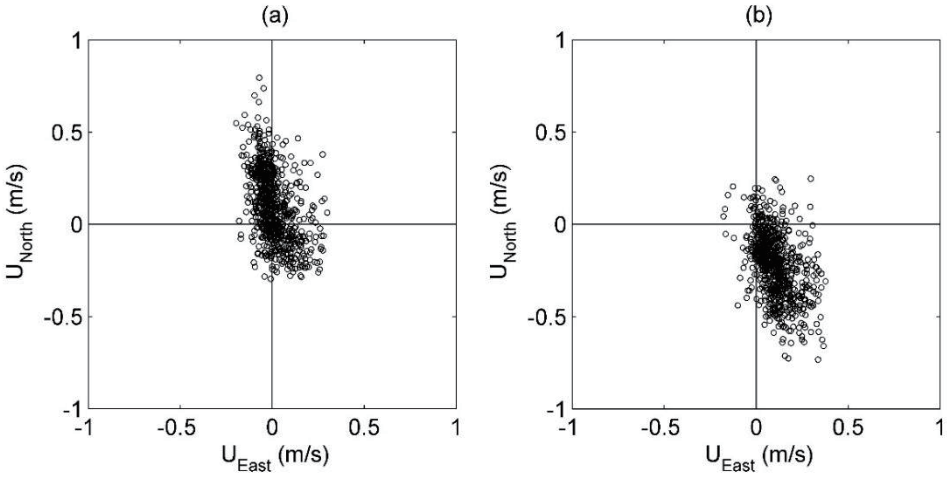

Figure 6. (a) Simultaneous in-situ current information for the radar echo bands bending toward the north; (b) Simultaneous in-situ current information for the radar echo bands bending toward the south.

In addition to the periodic motion of thermal plumes, which are influenced by the surface current, we also detected patterns of ocean fronts, which are induced by the thermal plumes. Ocean fronts are natural boundaries between waters with differing properties. Drastic changes in the properties of oceanic waters of clearly frontal origin, such as sharp interfaces between warm and cold masses of water, were known to seamen since at least the 15th century (Ginzburg and Kostianoy, 2008). Baschek et al. (2006) noted that the flow field of an ocean front is important because the surface convergence zone determines the point where surface waves break, and hence the location of bubble injections.

Fronts can be formed by three different mechanisms: inflow of dense water from an adjacent channel, flow separation past a headland, or flow over a shallow sill. The ocean front mechanism noted in our surface radar image cases is similar to the first of these processes. The thermal effluent flowing from the drain outlet is warmer and less dense than the coastal water. The interaction between the cooler coastal waters and the warmer jet enhances both wave breaking and air-sea gas exchange. At the front, the surface is rougher, producing a distinct bright line on the image. Some studies have confirmed the feasibility of ocean front detection from radar images. Askari et al. (1996) examined X-band radar echo intensity changes in the surface roughness associated with oceanic features in the low-angle grazing scattering regime. Their results also showed that the step changes in radar cross-section modulations are associated with either thermal stability-induced stress variations or variations in current velocity. Compared to their study, which used shipboard radar, the land-based radar we applied can extract the movement information of the front. Figure 7 presents the image cases for four continuous hours. We see an ocean front (indicated by a gray arrow) moving from the drain outlet of the power station. An obvious front pattern is starting to emerge from the area in front of the drain outlet at 19 o'clock. One hour later, we can see that the ocean front pattern is spreading. At 21 o'clock, the front of the plume becomes nearly arc-shaped with a radius greater than 2 km. At 22 o'clock, the front is approximately 3 km from the drain outlet. At 19 o'clock, we also see another front pattern (black arrow) in front of the harbor mouth. This is due to the interaction between the coastal water and the body of water inside the harbor. During ebb tide, the water inside the harbor flows into the coastal waters through the harbor mouth. The contraction at the harbor mouth increases the current and results in the ocean front in this area.

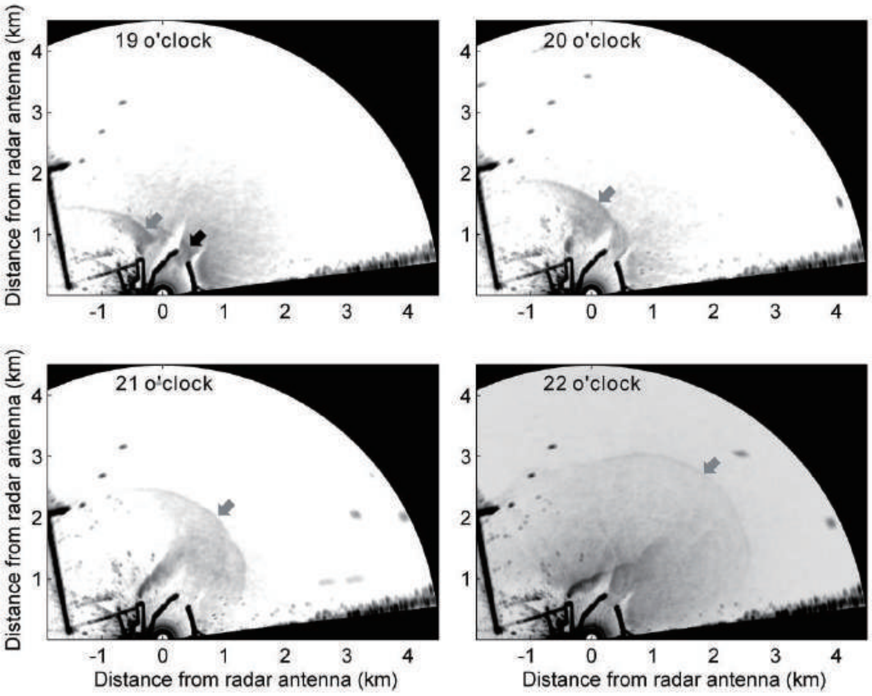

Figure 7. Motion of the ocean front within a four-hour period.

5 INFLUENCE OF ENVIRONMENTAL FACTORS IN DETECTING THE THERMAL PLUME PATTERN

Although we have confirmed the possibility of detecting the thermal plume with X-band radar images, we also noticed that the radar echo intensity of the thermal plume is variable with time. This implies that the thermal plume patterns may not be detected clearly under some circumstances. Radar backscattering at low grazing angles plays a specific role in the scattering of electromagnetic microwaves by the rough sea surface. The Bragg wave is a key in radar backscattering from the sea surface. The Bragg wavelength of X-band radar is approximately 1.5 cm. Sea surface wavelengths less than 4 cm are sensitive to wind speed. Radar backscattering enhanced by ripples is modulated by wind-generated waves (Long et al., 1996; Nieto-Borge et al., 2008). The causes for ocean roughness variance vary from near-surface wind speed fluctuations to stability effects dependent on the temperature differences between the air and upper layer of water (Kanevsky, 2008). Askari et al. (1993) reported that changes in atmospheric stratification resulting from sea surface temperature variations produce changes in surface wind stress; hence, the change in surface roughness driven by stress variability is one of the dominant ingredients in imaging frontal boundaries. However, stratification conditions in the lower marine atmospheric boundary layer are mainly influenced by the air-sea temperature difference (Dankert and

Horstmann, 2007). Here, we discuss how atmospheric and sea surface environmental factors may influence the detection of the sea surface thermal effluent.

In our experimental sites, not only the wind features but also the air and sea temperatures are quite different in different seasons. In our study of the influence of environmental features on the detection of the thermal plume pattern, we first discuss the image cases for different seasons. The radar image cases from two experimental sites mentioned in Figure 1 are used here. We classify our radar image cases based on different seasons as shown in Figure 8. In the two different experimental sites we found that the radar echo intensities are stronger in autumn and winter than in the other seasons. Those in spring and summer are mainly below 0.05, but mostly over 0.05 in winter. There are two explanations for this phenomenon. During the late autumn and winter seasons, water temperatures are often warmer than the air temperature. This stratification enhances radar backscatter from the rough sea surface. In addition, the sea states in our study sites are dominated by different monsoon systems. During the late autumn and winter, the strong northeasterly wind has speeds as high as 19 m/s. Compared to the winter monsoon, the summer monsoon is much weaker and blows from the southwest.

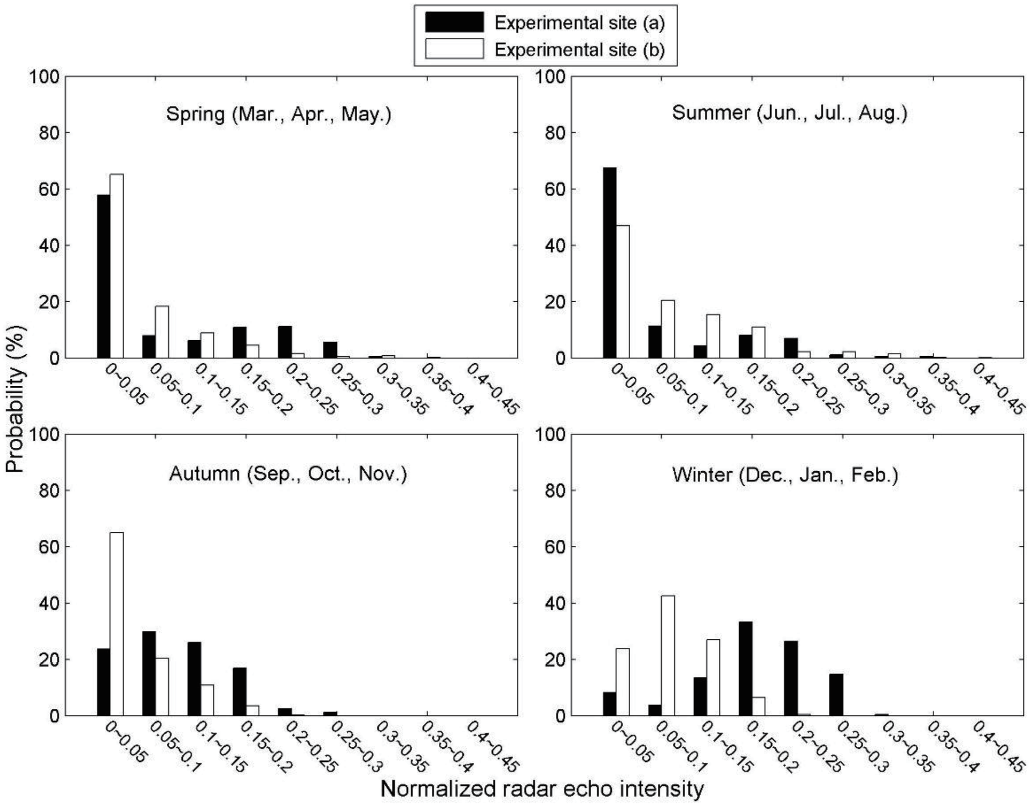

Figure 8. Radar echo intensities from the sea surface in different seasons.

To determine the influences of environmental factors on the heated water surface, we collected radar images and simultaneous air and sea surface temperature data from the moored buoy mentioned above in Figure 1(b). Although no thermal plume exists within the Figure 1(b) study site, the temperature data are still useful for clarifying the sea surface backscattering mechanisms under different temperatures. In focusing on temperature, we cannot ignore the influence of wind on radar backscattering. We therefore collected the radar images and air and sea surface temperature records under different wind speeds. The mean wind speeds are classified on the Beaufort scale (World Meteorological Organization, 1988). As shown in Figure 9, sea surface radar backscattering is slightly related to the air-sea temperature difference (D_{AS}). At low wind speed (Beaufort numbers 1–3), we could not determine a relationship between temperature difference and radar echo intensity. At high wind speeds (Beaufort numbers 4–9), the radar echo intensities are often weak if the sea surface temperature is lower than the air temperature. On the other hand, we observe more examples of strong radar echo intensity when the sea surface temperature is higher than the air temperature. Strong winds often occur in winter in our study area. This is why we see very few examples in which $D_{AS} \geq 0$. The sea surface plume temperatures are always higher than the sea surface temperature, which can enhance the radar echo intensity.

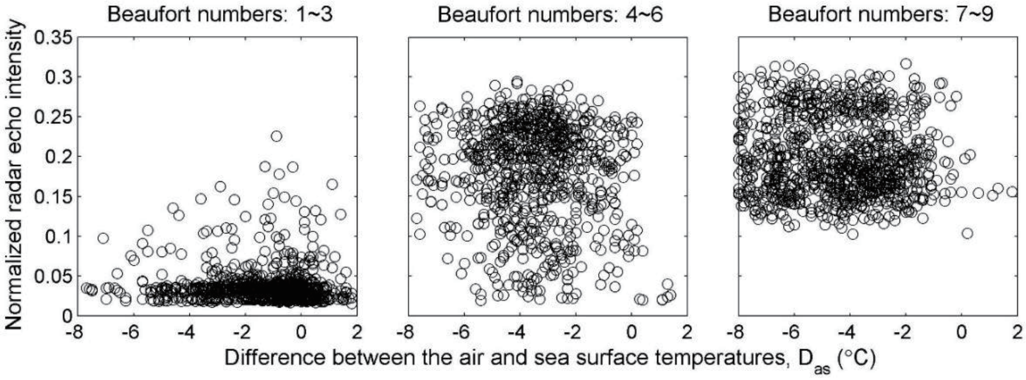

Figure 9. The influence of air-sea temperature differences on sea surface backscattering.

Figure 9 shows that at weak wind speeds the high D_{AS} cannot induce a strong radar echo intensity. The influences of wind speed are much greater than the effects of air-sea temperature differences. Plant et al. (2010) reported that radar echo intensity increases with wind speed. The ocean surface roughness caused by air-sea interactions is a dominant factor in the radar imaging of the ocean surface. It is thus necessary to clarify the hydrodynamics of the sea surface and the nature of the coupling between the sea surface and the wind.

Regarding the interaction between the microwaves and the sea surface, Alpers et al. (1981) reported that radar sea-surface imaging mechanisms are dominated by the tilt (geometric) and hydrodynamic modulations of the backscatter. Tilt modulation is related to the slope of surface waves. For radar backscatter events in areas of high steep-wave incidence, direct reflection from large sea waves is the primary source. In addition, high-frequency small-scale waves, which generate sea surface roughness, are influenced by large gravity waves through hydrodynamic modulation (Kanevsky, 2008). Moreover, the direction of current flow at the drain outlet is often opposite to the wave direction. The resulting countercurrent will increase the slope of the wave profile, and the steeper wave enhances the direct reflection of the radar electromagnetic waves.

The radar echo is reported to also depend on the wind direction, with the X-band radar backscatter being greater for upwind conditions (Nieto Borge and Guedes Soares, 2000). The radar image data and simultaneous wind and wave data in the Figure 1(a) experimental site are used here. We studied the relationship between wind/waves and radar echo intensity from the sea surface thermal plume. Compared to other studies which analyzed sea surface echo intensities under different wind conditions, we focused on the ratio of echo intensity between the area of thermal plume and the area without any plume. This ratio will help us understand the effects of wind on the detection of plume patterns. Because it is difficult to calculate radar echo intensity from the entire oscillating thermal plume band, we selected a smaller sub-image from the sea surface image that was very close to the drain outlet. The sub-image is defined as sub-image (A) in Figure 10.

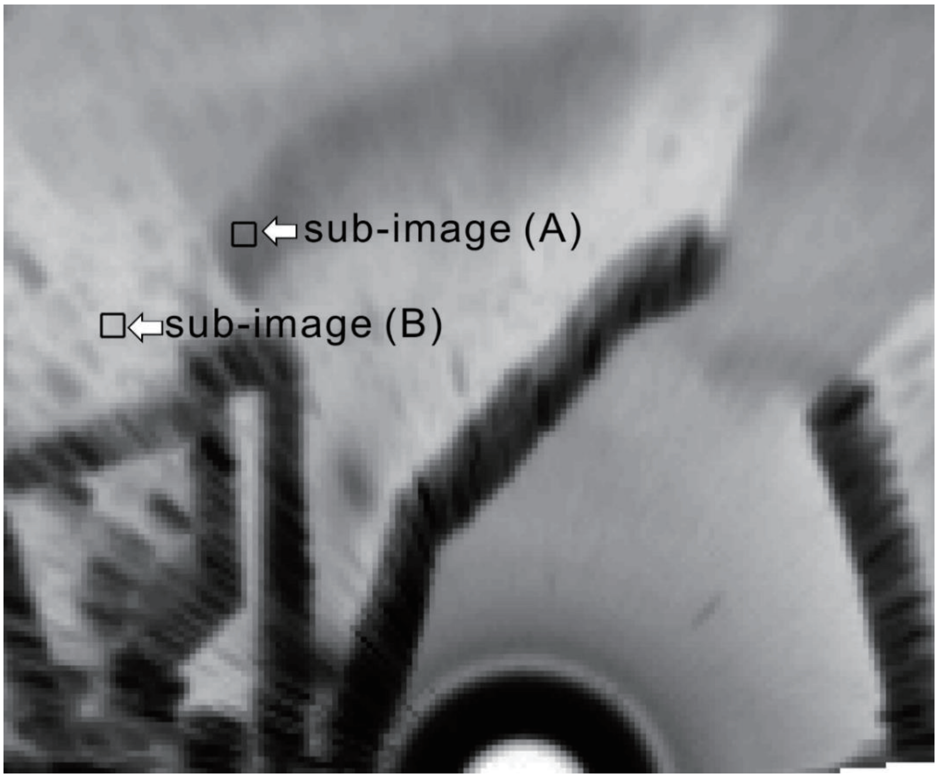

Figure 10. Locations of sub-images (A) and (B).

The size of sub-image (A) is 5 × 5 pixels. Because of their location and size, sub-images (A) are always within the area of the thermal plume. To understand the difference between the radar echoes from the thermal plume and the non-thermal plume area, we selected another 5 × 5-pixel sub-image (B) that is not located within the thermal plume radar echo band. Note that the distances of sub-images (A) and (B) from the radar antenna are made the same to avoid radar echo decay. We calculated the ratio of radar echo R_I between the two different sub-images:

$$R_I = \sum_{y=1}^{5}\sum_{x=1}^{5} I_A(x,y) \Big/ \sum_{y=1}^{5}\sum_{x=1}^{5} I_B(x,y) \qquad (2)$$

where $I_A(x,y)$ and $I_B(x,y)$ are the radar echo intensity within sub-images (A) and (B), respectively. After calculating R_I from each image case, we compared the value of R_I with the simultaneous wind and wave data. Over 3,000 different image cases were used to address this issue.

Figure 11(a) presents the relationship between wind speed and R_I . Although R_I increases with wind speed, a strong correlation between the two is not apparent. The distribution of R_I values is quite scattered at low wind speeds and less scattered when wind speed is higher, showing the influence of wind speed on the distribution of R_I . The relationship between wind speed U and R_I can be fitted to an exponential curve. Daley et al. (1971) reported that the relationship between wind speed and X-band radar cross-section obeys an exponential law. Note that the parameter R_I in our study is defined as the ratio of the thermal plume radar echo to the radar echo without the thermal plume. Figure 11(a) reveals that the exponential relationship between wind speed and the thermal plume radar echo is stronger than in the case of the non-thermal plume radar echo.

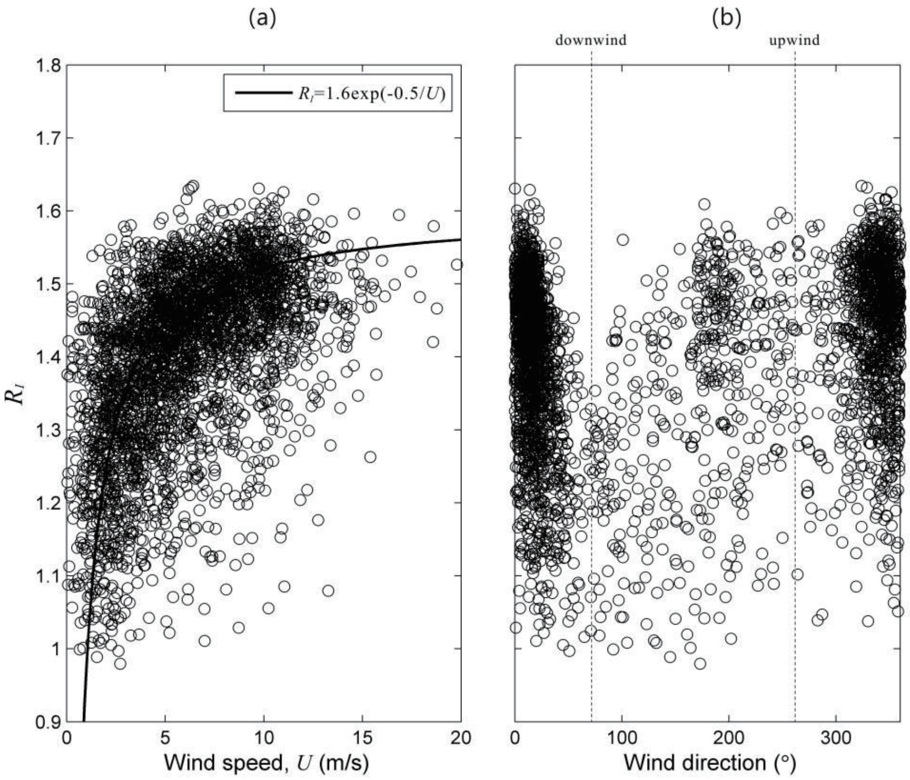

Figure 11. The relationship between the wind and R_I .

In addition to wind speed, many observers have noted that the upwind sea echo is generally greater than the values obtained from other viewing aspects (Skolnik, 1969). Figure 11(b) presents the relationship between wind direction and R_I . The relationship between wind direction and radar azimuth also appears to influence the value of R_I . Compared to the downwind cases, we observed greater R_I data more frequently in upwind situations, indicating that the thermal plume radar echo is more sensitive to upwind conditions than the non-thermal plume radar echo.

Compared to the wind, the exponential relationship between the wave heights andr R_I is not so obvious (Figure 12). However, higher values ofr R_I always occur under conditions of greater wave height. Larger waves thus contribute to the enhancement of the thermal plume radar echo. Unlike the relationship between wind direction andr R_I , there is no obvious connection between wave direction andr R_I . Due to bathymetric factors, the wave directions are concentrated from the west. It is difficult to clarify the influence of wave direction on the radar echo from our data set.

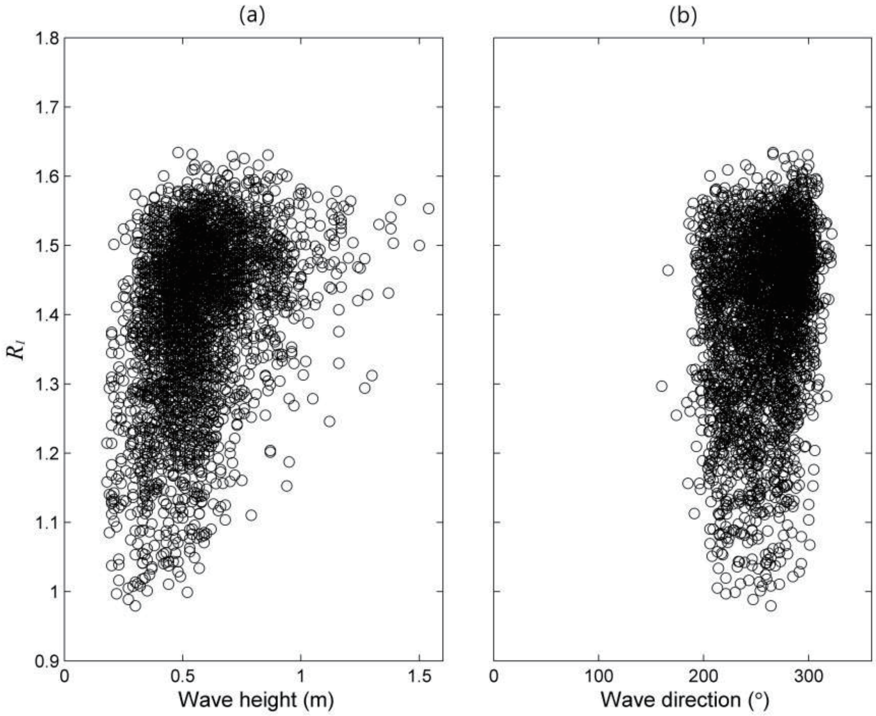

Figure 12. The relationship between waves and R_I.

6 CONCLUSIONS

In addition to seawater temperature, the movement features of thermal plume are also important for evaluating the environmental effects of heated water discharge. Remote sensing is a useful way to detect the spatial distribution of the thermal plume. Compared to remote sensing by aircraft or satellite, the value of land-based radar technology lies in its ability to monitor coastal physical phenomena more frequently. High-resolution remotely sensed images obtained from land-based radar are more effective for tracking the plume motion continuously. We studied the patterns of a nearshore thermal plume from the sea surface images of land-based X-band radar images. We did not attempt to determine water temperatures from the radar image patterns. Instead, we extracted the movement information of the thermal plume, which is important for coastal management.

Field radar images with simultaneous meteorological and sea-state data were used to study the plume patterns under different environment conditions. Although the in-situ sea surface temperature measurements of the thermal plume lasted only several hours, we were still able to confirm that a band with strong radar echo intensities on our image case was induced by the thermal plume. After analyzing the continuous image cases and the simultaneous in-situ sea surface current data, we verified that the movement features of a thermal plume are dominated by sea current speed and direction. Due to interactions between a less dense and warmer water injection from an adjacent channel into the cooler coastal waters, the thermal plume enhanced wave breaking and air-sea gas exchange. The interface between these two different water masses is seen as a rougher oceanic front that produced the distinct bright line on the radar image. The oceanic front located 3 km away from the radar antenna is still detectable in the patterns on our image cases.

Examining different image cases revealed that sea surface backscattering is affected by the seasons. Analyzing the image cases with different air-sea temperature differences and wind features revealed that a strong radar echo intensity occurs when the sea surface temperature is higher than the air temperature. Although a negative air-sea temperature difference enhances radar echo intensity, the latter is still not obvious when the wind speed is weak. Wind is a key factor that enhances the plume pattern on the X-band radar image. High wind speed as well as upwind conditions can both enhance the radar echo intensity of the thermal plume.

In summary, we have confirmed that the pattern of a thermal plume can be detected from X-band radar images. Plume motion information can be obtained by tracking continuous radar images. This information can be applied to verify the results of plume simulation based on numerical models.

REFERENCES

Alpers, W. R., Ross, D. B., & Rufenach, C. L. (1981). On the detectability of ocean surface waves by real and synthetic aperture radar. *Journal of Geophysical Research: Oceans, 86*(C7): 6481-6498. https://doi.org/10.1029/JC086iC07p06481

Askari, F., Donato, T. F., & Morrison, J. M. (1996). Detection of oceanic fronts at low grazing angles using an X band real aperture radar. *Journal of Geophysical Research: Oceans, 101*(C9): 20883-20898. https://doi.org/10.1029/96JC00999

Askari, F., Geernaeft, G. L., Keller, W. C., & Raman, S. (1993). Radar imaging of thermal fronts. *International Journal of Remote Sensing, 14*(2): 275-294. https://doi.org/10.1080/01431169308904337

Baschek, B., Farmer, D. M., & Garrett, C. (2006). Tidal fronts and their role in air-sea gas exchange. *Journal of Marine Research, 64*: 483-515. https://doi.org/10.1357/002224006778715766

Bau, H. Y., Wu, L. C., & Chuang, L. Z. H. (2013). Detection of Thermal Effluent Discharge Using Sea Surface Nautical Radar Images. *IEEE Geoscience and Remote Sensing Letters, 10*(3): 612-616. https://doi.org/10.1109/LGRS.2012.2215912

Borge, J. C. N., Rodriguez, G. R., Hessner, K., & Gonzalez, P. I. (2004). Inversion of marine radar images for surface wave analysis. *Journal of Atmospheric and Oceanic Technology, 21*(8): 1291-1300. https://doi.org/10.1175/1520-0426(2004)021<1291:IOMRIF>2.0.CO;2

Daley, J. C., Ransone, J. T., & Burkett, J. A. (1971). Radar Sea Return-JOSS I. Defense Technical Information Center / NAVAL RESEARCH LAB WASHINGTON DC.

Dankert, H., & Horstmann, J. (2007). A Marine Radar Wind Sensor. *Journal of Atmospheric and Oceanic Technology, 24*(9):1629-1642. https://doi.org/10.1175/JTECH2083.1

Frasier, S. J., Liu, Y., & McIntosh, R. E. (1998). Space-time properties of radar sea spikes and their relation to wind and wave conditions. *Journal of Geophysical Research: Oceans, 103*(C9): 18745-18757. https://doi.org/10.1029/98JC01456

Ginzburg, A. I., & Kostianoy, A. G. (2008). Fronts and Mixing Processes. In Nihoul, J. C. J., and Chen, C. T. (Eds.), *OCEANOGRAPHY: ENCYCLOPEDIA OF LIFE SUPPORT SYSTEMS* (Vol.1, pp.237-268). Eolss Publishers Company Limited.

Joongcheol, P. (2011). Numerical simulation of thermal discharges in crossflow. *2011 IEEE 3rd International Conference on Communication Software and Networks,* 328-332. http://dx.doi.org/10.1109/ICCSN.2011.6014906

Kanevsky, M. B. (2008). *Radar Imaging of the Ocean Waves*. Elsevier Science.

Lee, P. H. Y., Barter, J. D., Beach, K. L., Lake, B. M., Rungaldier, H., Thompson, H. R., & Yee, R. (1998). Scattering from breaking gravity waves without wind. *IEEE Transactions on Antennas and Propagation, 46*(1): 14-26. https://doi.org/10.1109/8.655447

Long, D. G., Collyer, R. S., & Arnold, D. V. (1996). Dependence of the normalized radar cross section of water waves on Bragg wavelength-wind speed sensitivity. *IEEE Transactions on Geoscience and Remote Sensing, 34*(3): 656-666. https://doi.org/10.1109/36.499745

Miller, S. (1977). The impact of thermal effluents on fish. *Environmental Biology of Fishes, 1*: 219-222. https://doi.org/10.1007/BF00000415

Mustard, J. F., Carney, M. A., & Sen, A. (1999). The Use of Satellite Data to Quantify Thermal Effluent Impacts. *Estuarine, Coastal and Shelf Science, 49*(4): 509-524. https://doi.org/10.1006/ecss.1999.0517

Nieto Borge, J. C., Hessner, K., Jarabo-Amores, P., & de la Mata-Moya, D. (2008). Signal-to-noise ratio analysis to estimate ocean wave heights from X-band marine radar image time series. *IET Radar, Sonar & Navigation, 2*(1): 35-41. https://doi.org/10.1049/iet-rsn:20070027

Nieto Borge, J. C., & Guedes Soares, C. (2000). Analysis of directional wave fields using X-band navigation radar. *Coastal Engineering, 40*(4): 375-391. https://doi.org/10.1016/S0378-3839(00)00019-3

World Meteorological Organization (1988). *Guide to Wave Analysis and Forecasting.* https://library.wmo.int/?lvl=notice_display&id=7700#.Y0kCI3ZBzGI

Plant, W. J., Keller, W. C., Hayes, K., & Chatham, G. (2010). Normalized radar cross section of the sea for backscatter: 1. Mean levels. *Journal of Geophysical Research: Oceans, 115*(C9). https://doi.org/10.1029/2009JC006078

Ramos, R. J., Lund, B., & Graber, H. C. (2009). Determination of internal wave properties from X-Band radar observations. *Ocean Engineering, 36*(14): 1039-1047. https://doi.org/10.1016/j.oceaneng.2009.07.004

Richards, M. A. (2005). *Fundamentals Of Radar Signal Processing.* McGraw-Hill Education (India) Pvt Limited.

Robinson, I. S., Ward, N. P., Gommenginger, C. P., & Tenorio-Gonzales, M. A. (2000). Coastal Oceanography Applications of Digital Image Data from Marine Radar. *Journal of Atmospheric and Oceanic Technology, 17*(5): 721-735. https://doi.org/10.1175/1520-0426(2000)017%3C0721:COAODI%3E2.0.CO;2

Ruessink, B. G., Bell, P. S., van Enckevort, I. M. J., & Aarninkhof, S. G. J. (2002). Nearshore bar crest location quantified from time-averaged X-band radar images. *Coastal Engineering, 45*(1): 19-32. https://doi.org/10.1016/S0378-3839(01)00042-4

Skolnik, M. I. (1969). A Review of Radar Sea Echo. Naval Research Laboratory.

Sletten, M. A., Marmorino, G. O., Donato, T. F., McLaughlin, D. J., & Twarog, E. (1999). An airborne, real aperture radar study of the Chesapeake Bay outflow plume. *Journal of Geophysical Research: Oceans, 104*(C1): 1211-1222. https://doi.org/10.1029/1998JC900034

Sylvester, J. R. (1972). Possible effects of thermal effluents on fish: A review. *Environmental Pollution (1970), 3*(3): 205-215. https://doi.org/10.1016/0013-9327(72)90004-3

Trizna, D. B., Hansen, J. P., Hwang, P., & Wu, J. (1991). Laboratory studies of radar sea spikes at low grazing angles. *Journal of Geophysical Research: Oceans, 96*(C7): 12529-12537. https://doi.org/10.1029/91JC00705

Yanagi, T., Sugimatsu, K., Shibaki, H., Shin, H. R., & Kim, H. S. (2005). Effect of tidal flat on the thermal effluent dispersion from a power plant. *Journal of Geophysical Research: Oceans, 110*(C3). https://doi.org/10.1029/2004JC002385

Young, I. R., Rosenthal, W., & Ziemer, F. (1985). A three-dimensional analysis of marine radar images for the determination of ocean wave directionality and surface currents. *Journal of Geophysical Research: Oceans, 90*(C1): 1049-1059.